

# Structure of Wall-Eddies at $Re_\theta \approx 10^6$

by

Scott E. Hommema and Ronald J. Adrian

Laboratory for Turbulence and Complex Flow  
Department of Theoretical and Applied Mechanics  
University of Illinois at Urbana-Champaign  
216 Talbot Lab, Urbana, IL 61801, USA

## ABSTRACT

A smoke visualization experiment has been performed in the first 3 m of the neutrally stable atmospheric boundary layer at very large Reynolds number ( $Re_\theta > 10^6$ ). Under neutral atmospheric conditions mean wind profiles are shown to agree well with those in the canonical flat plate zero-pressure-gradient boundary layer. The experiment was designed to minimize the temperature difference between the passive marker (smoke) and the air to insure that any observed structures were due to vortical, rather than buoyant motions. Data was acquired in the streamwise/wall-normal plane using a planar laser light-sheet and CCD cameras. Images obtained are strikingly similar to those observed in classical laboratory experiments at low to moderate Reynolds numbers and reveal large-scale ramp-like structures with downstream inclination of  $3^\circ$ – $35^\circ$  (see Figure 1). This inclination is interpreted as the hairpin packet growth angle following the hairpin vortex packet paradigm of Adrian *et al.* (2000). The distribution of this characteristic angle is shown to agree with the results of experiments at far lower Reynolds numbers, suggesting a similarity in structures at low, moderate, and high Reynolds number boundary layers. These results begin to suggest that the hairpin packet model is valid at high Reynolds numbers of technological interest.

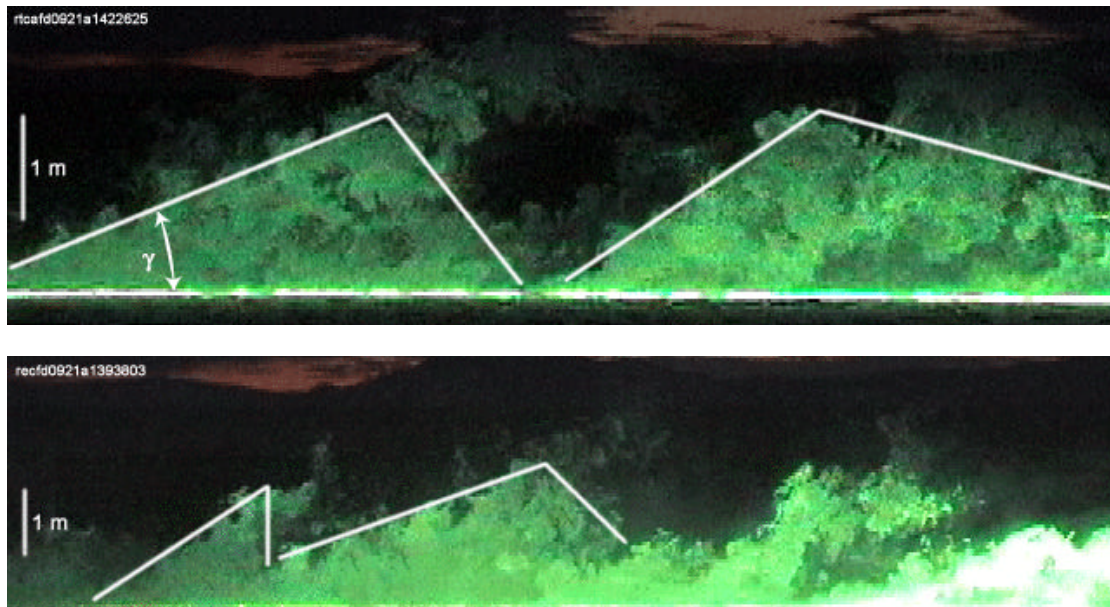


Figure 1. Two representative smoke visualization images in the first 3 m of the atmospheric boundary layer obtained using planar laser light sheet illumination. Flow is from left-to-right at  $Re_\theta = 9.2 \times 10^6$ . The approximate extent of the large scale structures has been indicated with white lines inclined at the hairpin packet growth angle  $\gamma$ .

## INTRODUCTION

Hot-wire anemometry and flow visualization experiments by numerous researchers have revealed the presence of large-scale coherent structures in turbulent boundary layers. Hydrogen bubble-wire visualizations by Smith & Metzler (1983) revealed low-speed streaks in the near-wall region. These streaks were shown to persist over large streamwise distances and their mean spacing was insensitive to Reynolds number. Smoke visualization experiments of Head & Bandyopadhyay (1981) indicate that the turbulent / non-turbulent interface at the outer edge of the boundary layer is sloped at a characteristic angle of approximately  $45^\circ$ . Bandyopadhyay (1980) used smoke visualization and hot-wire measurements to develop a simple model in which a coherent array of smaller structures inclined at  $45^\circ$  could explain the larger structures inclined at  $20^\circ$  observed in the outer region. Brown & Thomas (1977) used arrays of hot wires and inferred structures inclined at  $18^\circ$  from two-point correlations. The observed structures were shown to have streamwise extent of approximately  $2\delta$  and wall-normal extent spanning the entire boundary layer.

Particle image velocimetry (PIV) measurements by Adrian *et al.* (2000) (hereafter referred to as AMT) reveal ramp-like structures throughout the entire boundary layer. These structures, were shown to consist of 2 or more hairpin vortices each inclined roughly  $45^\circ$  to the wall which together form a ramp with characteristic growth angle of  $3^\circ$ – $35^\circ$ , depending mainly on distance from the wall. These results led the authors to develop the hairpin vortex packet paradigm (c.f. Figure 2) in which hairpin vortices form a hierarchy of large-scale structures. This model provides a possible basis for numerous structural features of wall turbulence including very-long low speed streaks, multiple u-momentum zones, and the presence of large-scale structures throughout the entire boundary layer.

All of the aforementioned work on large-scale structures has been at low to moderate Reynolds numbers as is evident from the summary of experimental parameters in Table 1. The physical model presented in AMT, summarized here in Figure 2, takes on increased importance if it can be shown to be valid at high Reynolds numbers where many devices of technological importance operate. The goal of this work is to investigate these large-scale motions in *high* Reynolds number boundary layer flows. We have chosen the atmospheric boundary layer as our high Reynolds number flow facility. Since the high Reynolds

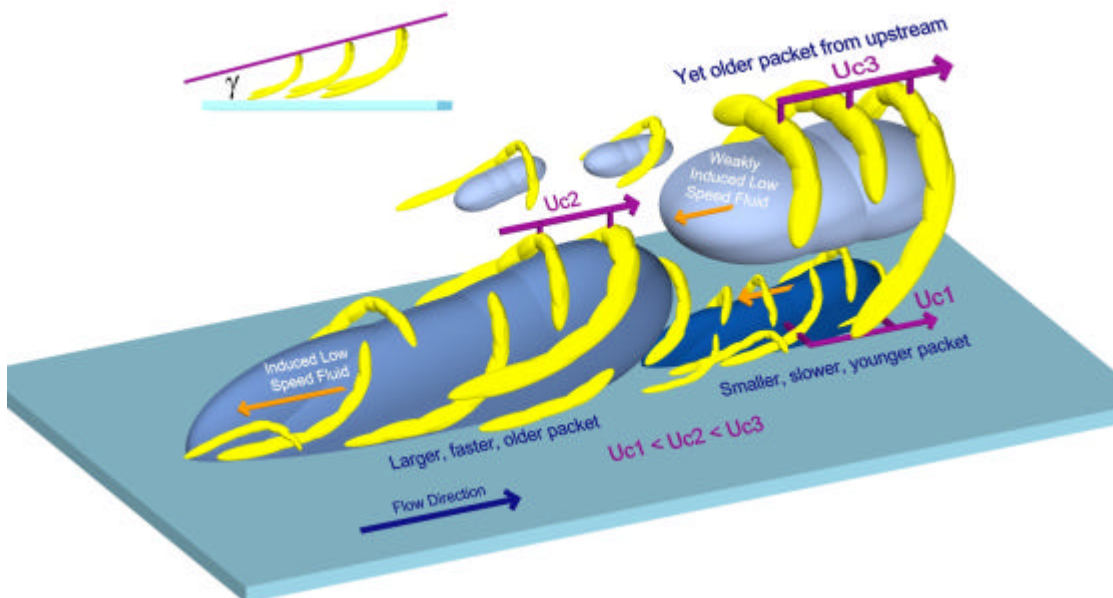


Figure 2. Hairpin vortex packet paradigm as proposed in AMT. Nested packets of hairpin vortices growing up from the wall align coherently in the streamwise direction to generate large regions of uniform streamwise momentum deficit. Packets grow at a characteristic growth angle  $\gamma$ , maintain coherence over large streamwise distances, and can be visualized as ramp- or wedge-like structures in visualization and PIV experiments.

number is due to the large length scale, the atmosphere affords extremely large Reynolds numbers ( $Re_\theta \geq 10^6$ ) without introducing the spatial resolution penalties associated with typical large Reynolds number apparatuses.

Table 1. Summary of Reynolds number range of previous investigations into large-scale coherent structures in turbulent boundary layers.

	$Re_\theta$
Adrian <i>et al.</i> (2000)	930 – 6,845
Head & Bandyopadhyay (1981)	500 – 17,500
Brown & Thomas (1977)	4,930 – 10,160
Smith & Metzler (1983)	740 – 5830
Present Study	1 – $9.2 \times 10^6$

## EXPERIMENT

A series of field tests were undertaken at the Surface Layer Turbulence and Environmental Sciences Test (SLTEST) facility in the U.S. Army Dugway Proving Ground, Utah during the period from September 13 to September 23, 1999. A combination of smoke visualization, hot-film anemometry (not presented here), and meteorological measurements were used to study the near wall (0–5 m) region of the atmospheric boundary layer over a smooth surface at near-neutral atmospheric stability. The test site is a large, flat, dried lake bed free of vegetation. The upwind fetch of approximately 24 miles in length has a slope of only 1/10000 and a surface roughness length of less than 3 mm. The topography and prevailing weather patterns favor northerly winds and as such, the instrumentation and test site facilities are installed with their upwind fetch to the north. A topographical map of the area with the test location indicated is included as Figure 3.

Smoke visualization was used to study coherent structures in the wall region (not to be confused with the near-wall region) of the atmospheric boundary layer. A number of different smoke types were tried but Naval type rescue smoke signals (floating orange smoke distress signal<sup>1</sup>) were found to provide the best results. Smoke was introduced via one of two injection plates. These plates (Figure 4) were mounted flush with the surface of the desert and care was taken to insure a smooth transition from the desert floor to the plate surface. During tests, orange smoke was issued from the spanwise slot in the downstream edge of the plate. The circular hole shown in the figure was used to access the cavity

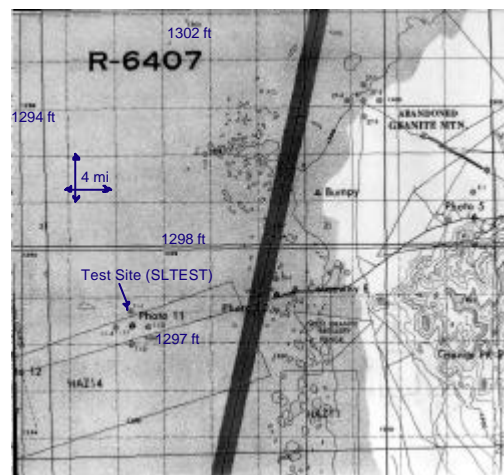


Figure 3. Topographical map of test site and surrounding area. Note the large unobstructed fetch North of the test site and uniform elevation.

<sup>1</sup> Manufactured by Norabel AB, Sweden and obtained through LHR Services & Equipment, (713) 943-2324.

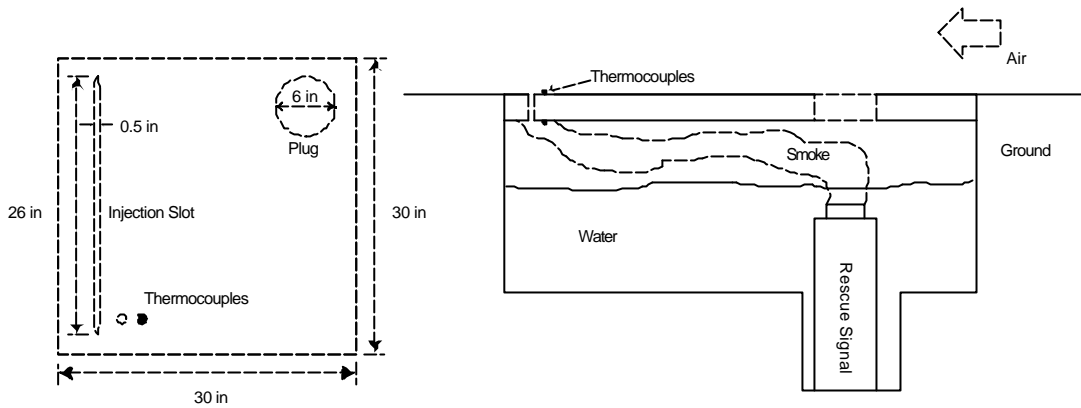


Figure 4. Detail view of the smoke injection plate and the water layer used to pre-cool the smoke used in visualization.

under the plate but was “plugged” during actual tests.

The primary goal of the field trials was to simulate a zero-pressure gradient turbulent boundary layer, therefore a neutrally stable atmosphere was desired for all measurements so that the unwanted effect of fluid buoyancy could be avoided. There was concern that the smoke used for visualization would be warmer than the surrounding air and this temperature difference would cause buoyancy effects. The experimental apparatus (smoke injection plates) was designed to minimize the temperature difference between the smoke and the air. This task was aided by the high ambient temperatures encountered in the desert-like conditions of the Utah salt flats and the design of the smoke injection plates.

The orange rescue signals are waterproof and work, at least temporarily, while underwater. A layer of water was added to the cavity below the orange smoke injection plate. The water's purpose was two-fold: first, the amount of smoke issued from the slot could be adjusted by varying the water depth in the cavity below the plate; and second, the water cooled the smoke before it was issued through the slot. Two thermocouples were placed in each plate, one above and one below, as shown in Figure 4 to monitor the temperature difference between the air and the smoke. Using this apparatus, the temperature difference was kept below 1 K during neutral atmospheric conditions. The size of the slot and the water depth together controlled the rate of smoke release and were varied until the smoke was issued with nearly zero vertical velocity as it left the slot.

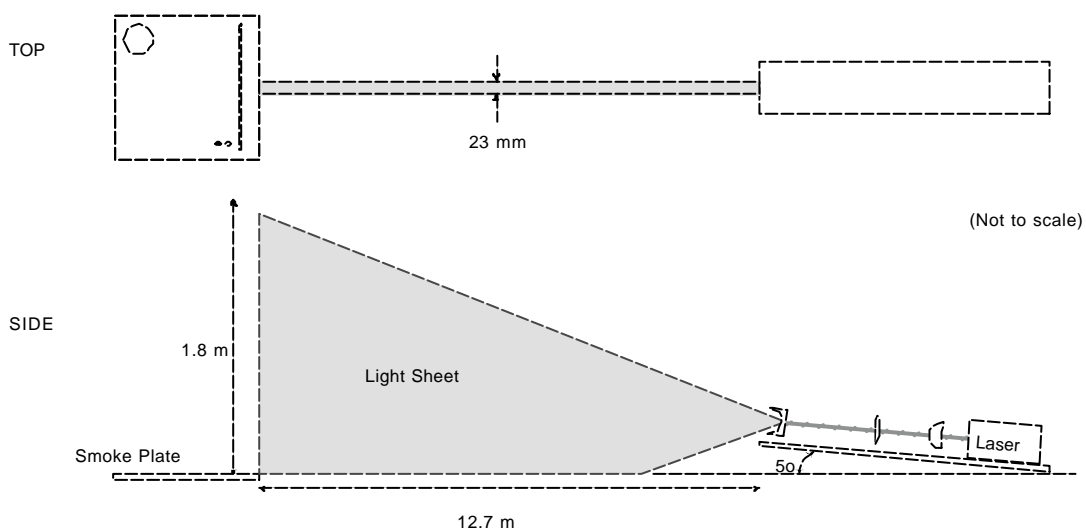


Figure 5. Light sheet and optics used in smoke visualization and their orientation with respect to the smoke injection plate. Mean air flow is from left to right.

A pulsed Nd:YAG laser (Gemini PIV by New Wave Research) was used to illuminate the smoke in a streamwise / wall-normal plane. Both heads of the double-pulsed system were fired simultaneously giving 240 mJ of total energy (532 nm) per pulse. The circular laser beam was passed through a spherical lens and two cylindrical lenses to form a planar light sheet of 2–3 mm maximum thickness oriented as shown in Figure 5. The laser heads and optics were mounted on a rigid plate which could be rotated with respect to the ground. The light sheet grows with increasing distance from the sheet-forming optics as suggested by the figure. Uncorrected, nearly half of the light sheet is obstructed by the ground. Rotation of the laser heads and optics by approximately 5–15°, minimizes this “wasted” light energy.

Digital camcorders (Sony model DCR-TRV8) mounted on tripods were used to record the smoke images in color. These camcorders use a 640 × 480 pixel CCD array and record on MiniDV digital tape in NTSC color at 30 interlaced frames per second. Unfortunately, there was no straightforward way to synchronize the framing of the cameras with the lasers firing at 15 Hz. As a result, the film sequences are characterized by alternating segments of exposed and unexposed frames corresponding to periods of time when the cameras and laser are in and out of phase, respectively.

A number of instruments were used to characterize the boundary layer. A 3 m instrument tower was used to support an array of four cup-and-vane anemometers (R.M. Young model 03101-5). A thermocouple probe was placed at each anemometer location to record air temperature. Instantaneous wind direction at 3.2 m from the wall was available from a digitally encoded wind vane (R.M. Young model 03001-5 Wind Sentry). Data from the four thermocouples, four anemometers, and wind vane were recorded at 0.2 Hz using a Campbell Scientific (Logan, Utah) model CR23X data logger.

The thermocouple probes were unshielded and un aspirated. As a result, it is probable that direct sunlight adversely affected their reading of absolute temperature. Since the temperature measurements are used to determine vertical temperature gradients rather than absolute temperature profiles, these errors did not cause any problems. A shielded and aspirated probe was available within the datalogger itself to supply the cold junction temperature for the thermocouple data reduction and the true air temperature. A floating drag plate was available from Prof. Joseph Klewicki at the University of Utah to determine wall shear stress and subsequently, friction velocity. The instrument consists of a 2.4 m diameter circular disk mounted flush with the desert floor, floating in a pool of water. Three force transducers mounted on the perimeter of the disk were used to record the force transmitted through the plate as a function of time (sampled nominally at 1 Hz) which was used to compute the wall shear stress and friction velocity.

Additional instrumentation was provided by the Dugway Proving Grounds. Four quartz thermometers were used to continually record the temperature at ground level, 0.25 m, 0.5 m, and 1 m above the surface. Unlike the instruments mounted on the tower, these instruments were radiation shielded and provide a more accurate measure of the true air temperature. An array of two, three-dimensional sonic anemometers (positioned at 1.75 m above the ground surface) continually measured the three dimensional wind velocity and vertical heat flux,  $\overline{w'\theta'}$ , which was used to help evaluate atmospheric stability.

## RESULTS

### Boundary Layer Characterization

The most critical parameter in this experiment was the stability of the wall region. A temperature-time history (approximately 6 hours) was recorded by the quartz thermometers for each of the four days in which data was collected and indicate that during the time period from 1850 to 2200 on September 15, the difference between the temperatures recorded at the ground and 1 m levels is less than 2 K. Between 1900 and 2200 the temperature difference is less than 1 K. Similarly, we find a temperature differential of less than 1 K from 1920 to 2200 on September 20, from 1900 to 2150 on September 22, and from 1900 to 2100 on September 23. Measurements obtained from the tower-mounted thermocouples, indicate that during the times in question the vertical gradient in temperature was less than 0.5 K/m for at least the first 3 m. Both results indicate that neutral conditions were realized.

A better measure of the boundary layer stability is the vertical heat flux,  $\overline{w'\theta'}$ , which is plotted in Figure 6 as 20 minute averages for the four days of interest. A positive heat flux indicates that warm fluid is being transported upwards, away from the wall, giving rise to unstable conditions. A negative heat flux indicates that warm fluid is being transported downwards giving negative stability. Neutral conditions are approached as the vertical heat flux approaches zero. We see from the figure that the heat flux is very nearly zero just around dusk, from approximately 1900 to 2100 hours, for each of the four days in question.

The bulk of the data collected during the experiment was taken during the time period 1800–2200 hours on Sep. 15, 20, 22, and 23 when the atmosphere was under nearly neutral stability. The streamwise velocity profile during this time period is presented in Figure 7 in terms of wall variables. The velocity was obtained from the cup-and-vane anemometers and scaled using friction velocities obtained from the drag plate measurements. Two log-law fits have been included for comparison, corresponding to a smooth wall and a surface with a roughness length of 0.3 mm, respectively. We find that the majority of the data collapse well. The outliers at low  $y^+$  are likely due to deviations in the wind direction as the lowest cup and vane anemometer falls in the wake of the instrument tower's supports during times when the wind is not Northerly. The three lowest points were excluded to compute the log-law fit. The outliers at large  $y^+$  are probably due to inaccuracies in the drag plate which develop as it contracts and expands with temperature variations but have been included in the curve fit.

It appears that the atmospheric boundary layer, during the near-neutral conditions considered, closely resembles a laboratory zero-pressure gradient turbulent boundary layer. A summary of the typical relevant boundary layer parameters is included in Table 2. Also included, for reference, are the equivalent parameters for a laboratory scale experiment performed by Tomkins (1997) at the University of Illinois. In the current study, the boundary layer thickness,  $d$  and free stream velocity,  $U_{\infty}$ , were conservatively estimated from mini-sodar data which was available for the first 200 m of the boundary layer (the actual extent of the boundary layer may have been 1 km or more). The main conclusion to be drawn from Table 2 is that the atmospheric boundary layer affords over a thousand-fold increase in Reynolds numbers with a three-fold reduction in required resolution (as evident by comparison of  $y^*$ ).

Table 2. Typical atmospheric boundary layer parameters in the current experiment for the period September 15, 20, 22, and 23, 1999 and the laboratory scale experiment of Tomkins (1997).

	Atmosphere	Laboratory
$d$	200 m	83.1 mm
$q$	14.2 m	10.4 mm
$U_{\infty}$	9.7 m/s	11.4 m/s
$y^*$	150 $\mu\text{m}$	37.5 $\mu\text{m}$
$U_t$	0.1–0.3 m/s	0.41 m/s
$\text{Re}_d$	$129 \times 10^6$	61,863
$\text{Re}_t$	$1.3 \times 10^6$	2,227
$\text{Re}_q$	$9.2 \times 10^6$	7,705

### Image Processing

Images recorded on the digital camcorders were time indexed by frame so that they can be matched with data taken with the other instrumentation. The raw images from the video were de-interlaced, adjusted for contrast, and the image backgrounds were removed digitally. One typical result has already been shown in Figure 1. In Figure 8a, the present results are compared with a laboratory PIV result. Note the presence of ramp- or wedge-like patterns that appear strikingly similar to those observed in laboratory experiments. The ramp-like structures indicated in Figures 1 and 8b have the same orientation and organization as those observed in the PIV results in the laboratory boundary layer. It should be noted that while the PIV results span the entire boundary layer thickness, the visualization only spanned roughly 3% of the boundary layer thickness. An image of the entire boundary layer in the current study would require a light sheet at least 200 m in height and a laser far more powerful than that used here.

The structures indicated in the figure were identified via an automated edge detection analysis. Prior to analysis, a mask was applied to each image to correct for uneven illumination caused by the growth and large extent of the light sheet. The resulting images were passed through a two-dimensional low-pass filter to remove the smallest scales (we are interested in the largest scales) and high frequency noise. Edges were then identified via a gradient search. The required spatial gradients were computed using Sobel operators (Jähne (1995)) for increased computational efficiency.

Guided by the observations discussed in the introduction, the result was projected onto straight lines angled with respect to the wall using a Radon transform. The resulting entity was considered to be part of a large-scale, coherent structure (previously referred to as a ramp) if five criteria were satisfied

- Wind direction was within  $\pm 5^\circ$  of the light sheet.
- Structure under consideration was fully contained within the light sheet and smoke-filled region. This assured that the detected edge was not due simply to the finite extent of the light sheet.
- Twenty minute average of vertical heat flux indicated neutral stability.
- “Front” and “back” of ramp was visible.
- There are at least two structures visible in the image. According to the hairpin vortex packet paradigm, these large-scale structures should appear in coherent groups so isolated structures were not counted.

The aforementioned procedure was used to identify “ramps” in 66 images spanning all four nights of testing. The images chosen for analysis were obtained during neutral atmospheric conditions with steady northerly winds but otherwise may be considered arbitrary and representative of the entire ensemble. For each structure, the angle made with the wall was recorded and the results are presented in the histogram shown in Figure 9b. Comparisons between structures identified via the automated analysis and those identified via simple visual inspection revealed few differences.

Note that the ramp growth angles vary from  $3.5\text{--}39^\circ$  with a mean of  $18.7^\circ$ . A ramp growth angle histogram computed from two-dimensional PIV data spanning the entire boundary layer thickness (Tomkins (1997)) with mean  $12.3^\circ$  is shown in Figure 9a for comparison. The results from the current study appear to be biased towards larger ramp angles. This is expected, since the method used here for feature extraction is more sensitive to the structures farther from the wall which have larger growth angles. Smaller structures, nearer the wall, are completely contained and masked by the larger structures farther from the wall. The PIV results used in the work of Tomkins (1997) were able to resolve vortices, and therefore ramps throughout the boundary layer without this limitation.

It should be noted that the hairpin packet growth angles reported here for  $Re_\theta > 1 \times 10^6$  agree with those reported by other researchers, namely Head & Bandyopadhyay (1981)  $-20^\circ$ ; Brown & Thomas (1977)  $-18^\circ$ ; Chen & Blackwelder (1978), Alving *et al.* (1990), MacAulay & Gartshore (1991)  $-15^\circ\text{--}90^\circ$  which were obtained at far more moderate Reynolds numbers. The structures observed in the current study are fully consistent with the hairpin packets in the vortex packet paradigm of AMT discussed earlier.

Tomkins (1997) indicated that ramp-like structures were observed in over 85% of the PIV realizations in a low to moderate Reynolds number boundary layer. This would suggest that the ramp-like structures discussed here represent a common, recurring feature of turbulent boundary layers at low to moderate Reynolds numbers. Considering that the 142 structures (ramps) described in Figure 9b were identified from only 66 images, a similar statement can be made regarding the results presented here—two or more ramp-like structures were observed in over 80% of the realizations obtained during neutral atmospheric conditions with steady winds. These structures appear to be a common and recurrent feature of turbulent boundary layers at *high* Reynolds numbers as well.

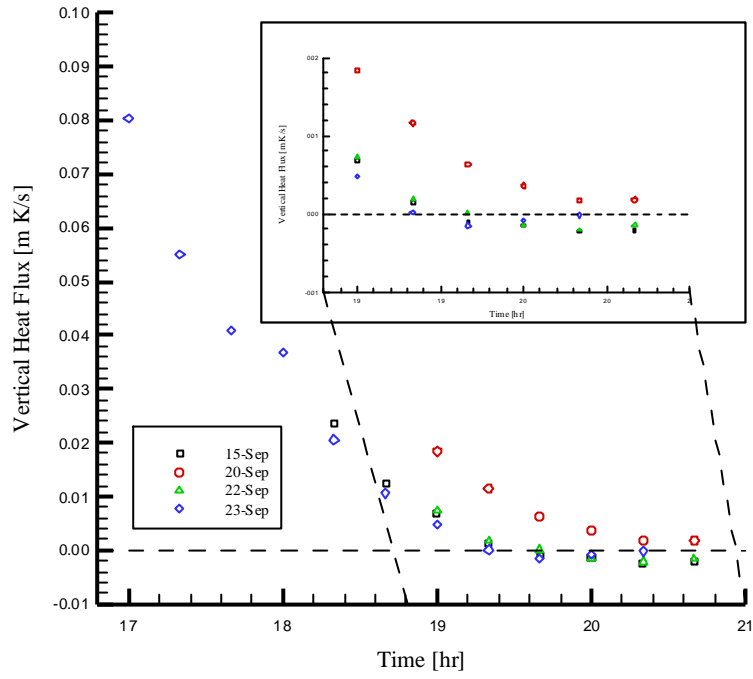


Figure 6. Vertical heat flux during testing periods as measured by a three-axis sonic anemometer.

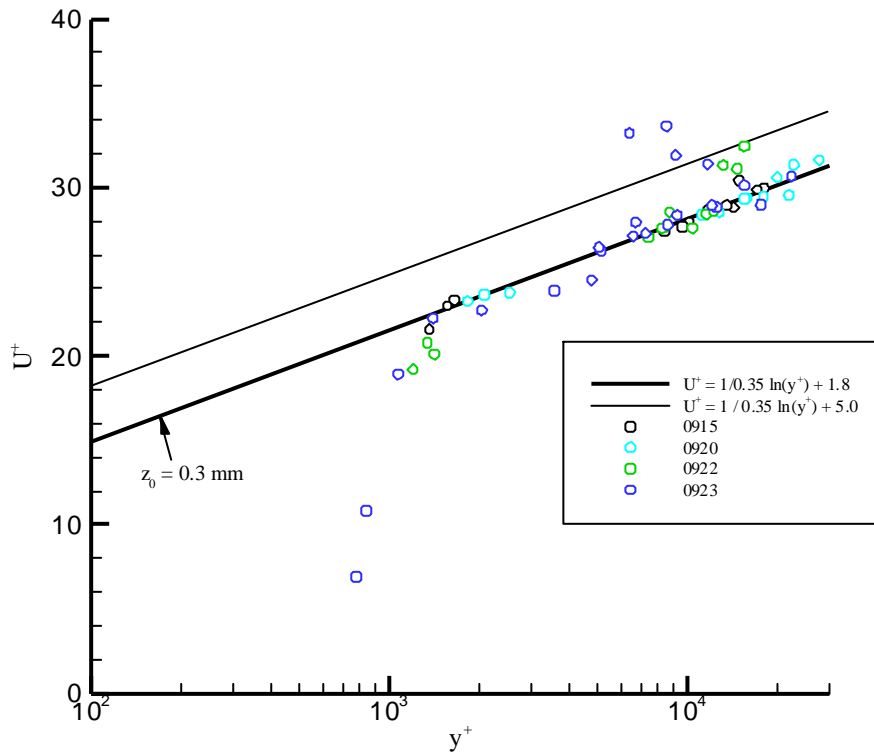


Figure 7. Streamwise velocity profile in inner (wall) variables.

## CONCLUSIONS

A field experiment has been conducted to examine large scale coherent motions in a zero-pressure-gradient turbulent boundary layer at very large Reynolds numbers ( $Re_\theta \geq 10^6$ ). The atmospheric boundary layer was found to generate very large Reynolds numbers while maintaining very reasonable spatial resolution requirements. Mean velocity measurements indicate that the atmospheric boundary layer resembles the canonical laboratory boundary layer during periods of time with steady winds and neutral thermal stability. Careful smoke visualization using a neutrally buoyant marker, in the first 2 m of the atmospheric boundary layer reveals structures similar in appearance and statistics (hairpin packet growth angle) to those observed in laboratory experiments at much smaller Reynolds numbers. This evidence coincides with the hairpin packet vortex paradigm of AMT and provides evidence that such a model can be extended to *high* Reynolds numbers of technological importance.

## ACKNOWLEDGEMENT

This work was supported by the Atmospheric Sciences division of the National Science Foundation.

## REFERENCES

- ALVING, A. E., SMITS, A. J. & WATMUFF, J. H. 1990 Turbulent boundary layer relaxation from convex curvature. *J. Fluid Mech.* **211**, 529–556.
- ADRIAN, R. J., MEINHART, C. D. & TOMKINS, C. D. 2000 Vortex organization in the outer region of the turbulent boundary layer. *J. Fluid Mech.*, to appear.
- BANDYOPADHYAY, P. 1980 Large structure with a characteristic upstream interface in turbulent boundary layers. *Phys. Fluids* **23**, 2326–2327.
- BROWN, G. L. & THOMAS, A. S. W. 1977 Large structure in a turbulent boundary layer. *Phys. Fluids* **20**, S243–S252.
- CHEN, C.-H. P. & BLACKWELDER, R. F. 1978 Large-scale motion in a turbulent boundary layer: A study using temperature contamination. *J. Fluid Mech.*, **89**, 1–31.
- HEAD, M. R. & BANDYOPADHYAY, P. 1981 New aspects of turbulent boundary layer structure. *J. Fluid Mech.*, **107**, 297–338.
- JAHNE, B. 1995 *Digital Image Processing*. Springer-Verlag, Berlin.
- MACAULAY, P. & GARTSHORE, I. P. 1991 A tentative model of outer layer structure in a turbulent boundary-layer developing on a smooth wall. In *Experimental Heat Transfer, Fluid Mechanics, and Thermodynamics* (eds J. F. Keffer, R. K. Shah & E. N. Ganic). Elsevier Science.
- SMITH, C. R. & METZLER, S. P. 1983 The characteristics of low-speed streaks in the near-wall region of a turbulent boundary layer. *J. Fluid Mech.*, **129**, 27–54.
- TOMKINS, C. D. 1997 A particle image velocimetry study of coherent structures in a turbulent boundary layer. Master's Thesis, University of Illinois.

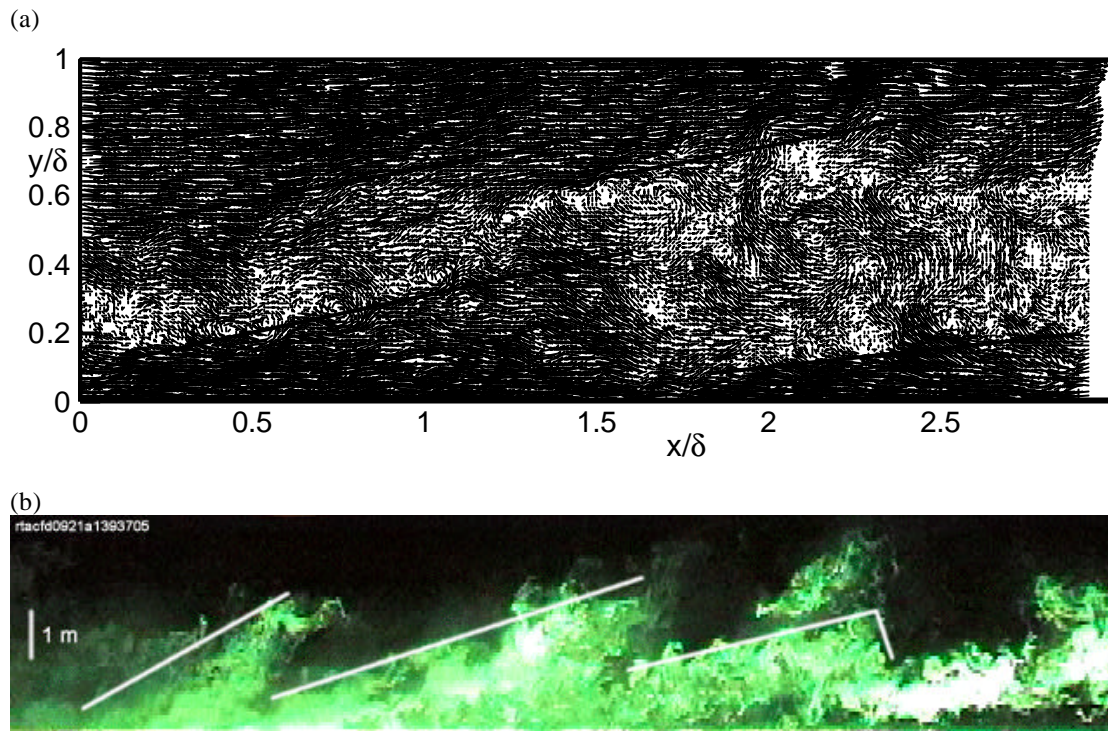


Figure 8. (a) PIV realization in the streamwise/wall-normal plane of a zero-pressure-gradient turbulent boundary layer at  $Re_\theta = 7705$  (AMT). Note that the entire boundary layer is shown. (b) Smoke visualization of the wall-region of the neutral atmospheric boundary layer at  $Re_\theta = 9 \times 10^6$ . In both cases, air flow is from left to right. A constant convection velocity of  $0.79 U_\infty$  has been subtracted from the vectors in (a). A hierarchy of ramp-like structures with similar orientation and structure is observed in both figures. The approximate extent of these structures has been indicated with solid lines.

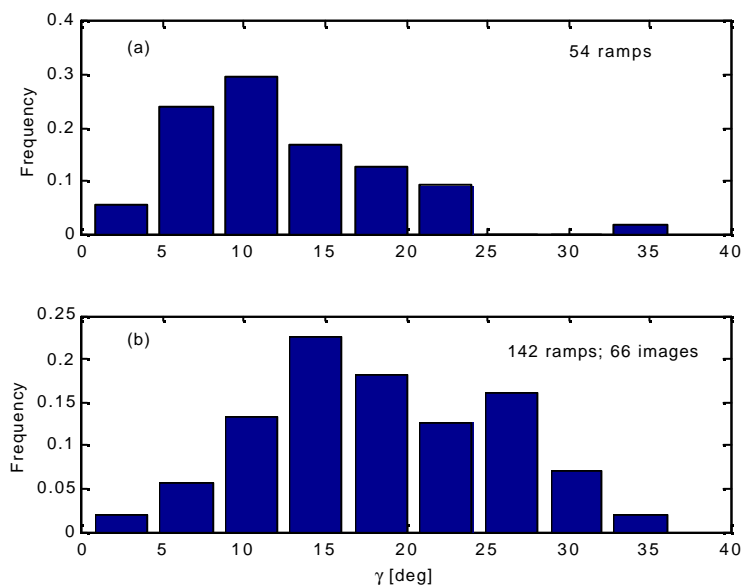


Figure 9. (a) Histogram of hairpin packet growth angles from laboratory boundary layer (Tomkins (1997)); (b) Histogram of hairpin packet growth angles from atmospheric boundary layer (present study).